Chapter 2

Experimental Methods and Instrumentation

2.1 Surface Analysis

In the field of surface analysis of polymers with biomedical applications, ToF-SIMS and XPS are the main complementary techniques used for the chemical characterisation of polymer surfaces. These techniques will be described in depth in this chapter both in terms of theory and the main experimental protocols used throughout the work presented in this thesis. A summary of different surface analytical techniques and their strengths can be seen in Figure 2.1 below

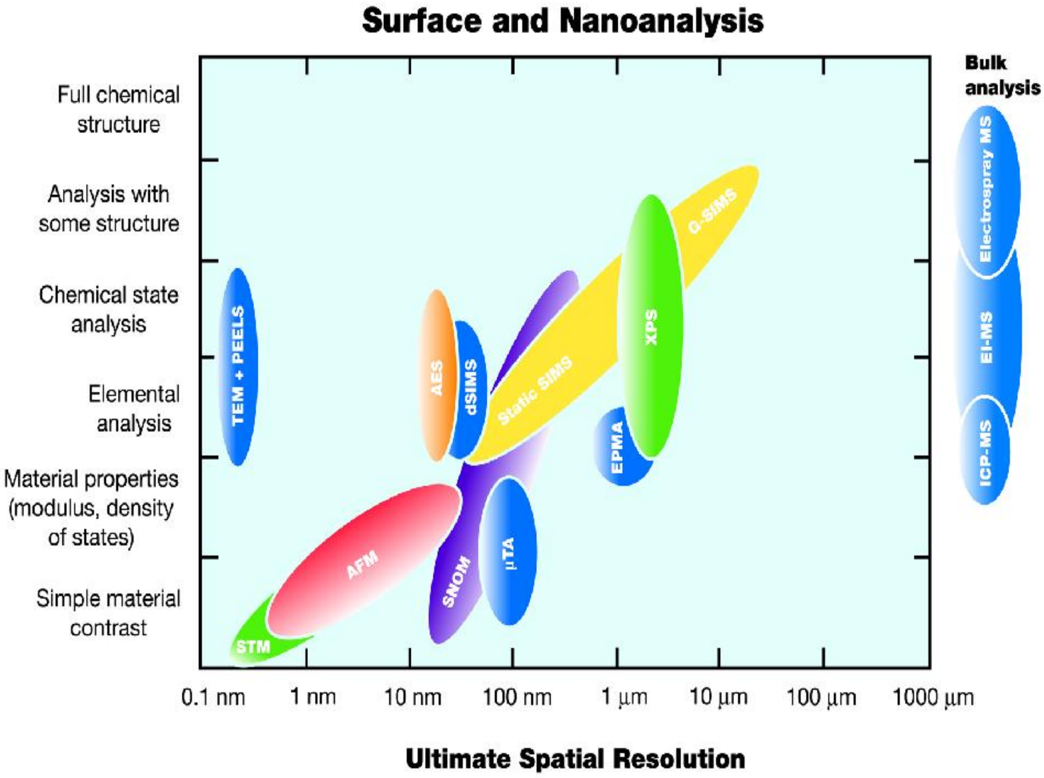

Figure 2.1 Graphical summary of the information content verses scale of different surface analytical techniques. (Reproduced with permission from Alex Shard, National Physical Laboratory ©).

Figure 2.1 shows how a general association exists between the highest spatial resolution and a reduced ability to conclusively identify the full chemistry of the analyte. Scanning tunnelling microscopy and atomic force microscopy are capable of Ångstrom spatial resolution. However, they are only able to provide simple phase contrast. Alternatively a technique such as ToF-SIMS shows the capability to provide detailed chemical analysis at the expense of spatial resolution. This is most apparent for ToF-SIMS whereby improving the spatial resolution has a linear reduction in improving our knowledge of the chemistry. Figure 2.1 also shows the versatility of techniques such as ToF-SIMS and the range of complementary techniques available for full chemical and structural surface analysis. The work in this thesis relies on the complementary nature of such techniques for the full characterisation of polymers for biomedical applications.

2.2 Sample Preparation.

Techniques such as ToF-SIMS and XPS are extremely sensitive to contamination. When producing samples for analysis it is vital to ensure at all stages of the production that all instruments and glassware being used are thoroughly cleaned prior to contact with any sample solutions or substrates. As ToF-SIMS is a highly surface sensitive technique (1-2 nm analysis depth) contamination of the surface can significantly influence the results. High purity solvents should be used to prepare sample solutions. Polyethylene gloves were used throughout the work discussed in this thesis. This was in order to avoid residue from commonly used nitrile gloves, which have been found to deposit a contaminant at the surface in the positive ion ToF-SIMS spectrum[1]. More common contaminants include poly(dimethyl-siloxane) (PDMS), a silicon grease, widely used in scientific machinery, which is often found to contaminate polymers. It is particularly troublesome for ToF-SIMS analysis as it migrates to the surface from the bulk attenuating the intensity of ions of significance. Even small concentrations can prove problematic[2, 3]. ToF-SIMS data are affected more by the presence of PDMS contaminants than are XPS data and this is likely to be a result of the increased surface sensitivity of ToF-SIMS over XPS[2, 3]. Elemental contamination, e.g., sodium, can affect the results generated by ToF-SIMS. As sodium is a highly electropositive element, small concentrations of sodium can overwhelm the detector reducing the intensity of ions specific to the sample from being detected[4]. In summary, considerable care should be placed in the preparation and handling of the sample solutions and the substrates to ensure they are free from contamination.

2.2.1 Thin Polymer Film Preparation.

For ToF-SIMS, depth profiling and XPS experiments, models of polymers with biomedical applications are often studied as thin films. It is imperative to have a uniform thickness across the sample in an effort to reduce the influence of topographical effects on the analysis[5] and also to ensure there are no contributions to the data from the underlying substrate. Spin casting is a commonly used method to achieve a flat thin polymer film for analysis. For the experiments cited in this thesis, a silicon wafer (Rockwood Electronic Materials, Derby, UK) measuring approximately 1 cm^2 was cleaned using piranha solution which is a 1:3 solution of hydrogen peroxide and sulphuric acid respectively (Sigma Aldrich, Dorset, UK). Piranha solution is a strong oxidant, removing all organic contaminants from the surface of the silicon substrate[6]. The wafer was carefully loaded onto the spin coater, paying strict attention to the positioning of the wafer. It must be centered over the o-ring where a vacuum is applied, so as to ensure as uniform a film thickness as possible shown in Figure 2.2.

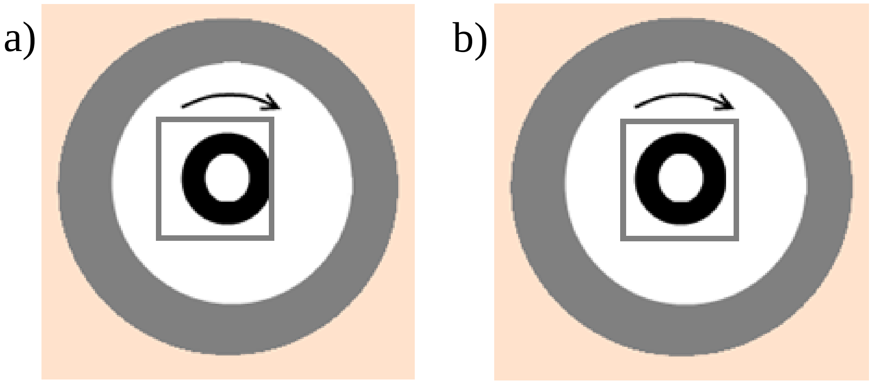

Figure 2.2 Schematic of a spin caster where the black ring represents the o-ring and the grey square represents the positioning of a silicon wafer. a) Incorrect positioning of wafer, b) correct positioning.

By misaligning the substrate slightly, on spinning of the sample solution onto the silicon substrate the non-centered rotation of the spin caster is responsible for forming a gradient in thickness. A 100 µL volume of the sample solution was pipette normal to the substrate mounted on the spin coater and spun at a spin speed of 4,000 revolutions per minute (RPM). All spin casting was undertaken for 60 s[7]. By reducing the spin speed the thickness of the resultant films was found to increase in a linear manner shown in Figure 2.3. This was determined by spin casting a solution containing PLA from chloroform onto a cleaned silicon wafer. An alpha-SE spectroscopic ellipsometer and analysed using the CompleteEASE software version 4.06 (J. A. Woollam Co., Inc., Lincoln, NE) was used to measure between 381 and 893 wave numbers.

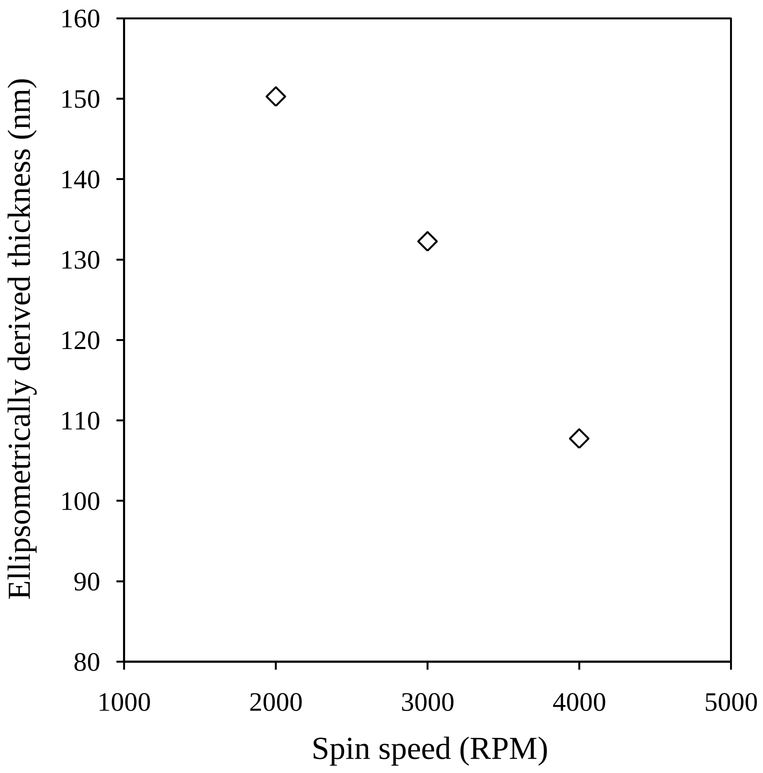

Figure 2.3 Spin casting speed against the ellipsometrically derived thickness for a PLA layer spun cast for 60 s from chloroform onto a piranha solution cleaned silicon wafer.

The polymer solution was formed by dissolving in a solvent such as chloroform that evaporates during the spin casting of the film. The solution is applied with a pipette onto the surface of the silicon wafer, covering it entirely before starting to spin cast. Spin casting has two major limitations. Firstly it has been shown in some cases the final layer is not at thermodynamic equilibrium and is not representative of thicker samples such as those used in drug delivery[8]. Secondly, it has been shown for certain polyurethanes, surface reorganisation occurred for a period of up to one week indicating an aging process of the sample after spin coating which could alter the analysis of the samples[8]. Knowledge of these limitations allows for considered analysis of resultant data to be made.

Dip coating is another sample preparation method that is capable of producing thin films. Dip coating involves dipping a substrate into a sample solution then extracting it and allowing it to dry before analysis. In dip coating the thickness may not be uniform over the entire sample area as shown by AFM studies leading to topographical effects in the analysis and the samples that may be thicker than desired and also less uniform in thickness across the surface[9]. As surface non-uniformity can affect ToF-SIMS and XPS[5] analysis for thin film casting, spin casting has been typically used for improved uniformity of thickness and topography.

2.3 Secondary Ion Mass Spectrometry

Secondary ion mass spectrometry (SIMS) is an ultra high vacuum (UHV) technique that measures the mass of ionised particles emitted from the surface of a sample when bombarded with primary ions. When bombarded with a high energy ion beam (in this thesis at 25 keV), a collision cascade results which ejects mostly neutral particles and some positive and negative ions (typically less than 1% of the sputtered material[10]). Secondary ion formation and generation is still not well understood but molecular dynamic (MD) simulations have been used to shed light on the formation of secondary ions from organic material[11-15]. The collision cascade is represented schematically in Figure 2.4.

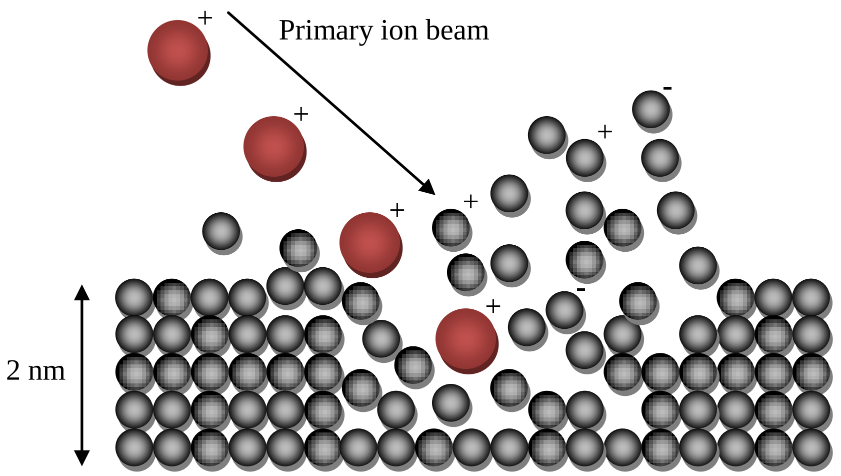

Figure 2.4 Schematic representation of the collision cascade in the sample for analysis caused by exposure to energetic primary ion bombardment (red).

The ions can be extracted and accelerated through a mass spectrometer[3]. This yields a mass spectrum that characterises the chemical composition of the top 1-2 nm of the sample surface, showing extremely high surface sensitivity. The spectra produced can be used to provide detailed information on the spatial distribution of components, structure[16] and orientation[17] of chemistries at the surface[18]. This thesis exploits the technique of static SIMS, where the primary ion dose is kept below 10^{13} ions cm^2 in order to cause minimal damage to organic samples. This value is derived through an approximation that one primary ion particle disturbs an area of 10 nm^2 and is termed the static limit. On reaching the static limit an area of 1 cm^2 would have been influenced by primary ion bombardment[10]. In this thesis, however, a primary ion dose of $\leq 10^{12}$ ions cm^2 is adhered to for surface studies in order to limit the damage dealt to the sample while maintaining intense molecular ion fragments.

The first SIMS instruments were developed in the early 1950s[19] and 1960s[20, 21] but it was not until the 1970s when it was adapted for use in fields such as the surface analysis of organic materials[10, 22]. Benninghoven and his group were successful in showing for the first time that with a low primary particle dose density (<1nA cm^{-2}) a mass spectrum could be produced, representative of the surface chemistry which adheres to the static limit[10, 22]. The low energy of the primary particles meant low secondary ion counts were observed with the quadruple mass analysers that were first used. Quadrupole mass analysers use four parallel rods in order to separate ions of a certain mass-to-charge ratio (*m/z*), a direct current (DC) and a radio frequency (RF) electric field is applied to a pair of these rods. An equal and opposite voltage is applied to the second pair. The switching of this field causes most ions to lose stability and collide with the rods. However ions from within a certain m/z range are transmitted to the detector[10, 23], as such the quadrupole mass analyser acts as a mass selective filter. By altering the electric field around the rods, a complete mass spectrum can be generated rapidly.

Currently the most popular mass analysers fitted to modern SIMS devices are time-of-flight (ToF) mass analysers. These function by accelerating secondary ions generated by pulses of primary ions to a given potential (V) in order to give all ions the same kinetic energy. As the heavier ions (*m/z*) will move slower with the same kinetic energy than a smaller one. The time (t) taken for each ion to impact on the detector, at the end of a 'flight tube' which has a known path length (L) can be measured[10]. A simple equation can be used to produce a ToF-SIMS spectrum and thus derive the mass of the ions shown in equation 2.1.

$$t = L\left(\frac{m}{2z\mathrm{V}}\right)^{\frac{1}{2}}$$

Equation 2.1

ToF mass analysers use the simplest mechanism for mass separation. Technological advances in computing have allowed for the time-of-flight for all ions extracted to be simultaneously recorded and compiled into a spectrum without the less efficient means of mass filtering found with quadrupole mass analysers where secondary ions outside of a given range are lost during the analysis. Such improvements on quadrupole mass analysers mean that ToF mass analysers are currently the most popular type of analyser used for SIMS and have been employed in all work shown in this thesis.

Modern SIMS instruments share the same major components, comprising an air-lock, main analysis chamber, primary ion gun, a mass spectrometer and the ion optical system which extracts ions of a given range of masses for transportation to the mass spectrometer for analysis (Figure 2.5). SIMS is capable of identifying all elements of the periodic table. In this thesis pressures as low as 7×10^{-9} Torr have been reached for analysis. An airlock system is used to allow the main chamber to be maintained at a low pressure. This facilitates consistent ion beam operation, reduces the occurrence of emitted ions colliding with gas phase molecules and reduces the opportunity for changes in surface chemistry during data acquisition[10].

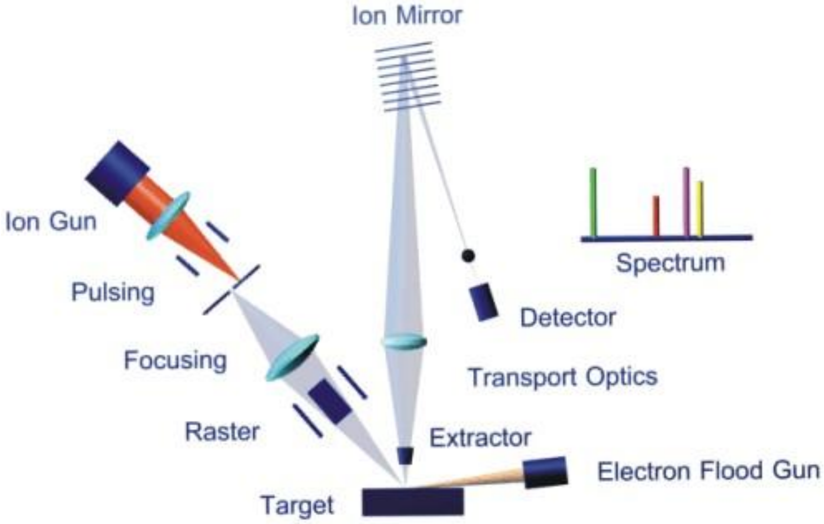

Figure 2.5 Schematic diagram showing reflectron design ToF – SIMS operation. © IONTOF.

The primary ion gun typically contains an ion source (usually a heated ion emitter e.g. bismuth), extractor, accelerator, mass/energy filter, stigmator, neutral elimination bend, focusing lens and facility for x-y raster capability. The ion produced in this process for bombardment is highly purified and of the correct energy to cause the collision cascade required. The results generated will depend on the mode the gun has been set to, whether a raster of a designated target area or a focused beam at one location[10]. There are four types of primary beam sources differentiated by the way the primary ions are produced; electron bombardment, plasma, surface ionisation and field ionisation sources. However, only field ionisation sources will be discussed here as this type has been used for analysis across all chapters in the thesis.

Field ionisation sources use a high electronic field in order to remove electrons from atoms of a liquid metal i.e. gallium or bismuth which flows over a tungsten tip with a radius < 1 µm where they are affected by the extraction field which can range between 10 and 40 kV. The extraction field causes the formation of a Taylor cone from which ions are stripped. Field ionisation sources typically have a very bright and focusable beam. As ToF systems require a pulsed beam and ion emission from a Taylor cone would be continuous deflector blanking plates are used to provide ns emission of ions in a pulsatile manner.

2.3.1 Ionisation and Matrix Effects.

Secondary ion formation is critically linked to the electronic state of the material being analysed as electron exchange processes are vital in ion formation. As such different ions will be more or less easily ionised depending on their interactions with the remaining material and how easily electrons are gained/lost. This can lead to variation in the secondary ion yield from different ions, these effects are termed matrix effects[10].

Quantification of the data generated by SIMS is made difficult by these matrix effects, for example, the silicon wafers used in this thesis as a substrate have a silicon oxide layer which causes an increase in the ion yield of silicon however if the oxide is removed (by sputtering) the silicon ion yield is ~ 70 times less[10]. Such effects are caused as particle emission and ionisation occurs 'simultaneously'. If ionisation occurred after the neutral particles had been emitted, the ion yield would be independent of the matrix allowing for more accurate quantification.

Techniques such as photon post-ionisation of sputtered neutrals using lasers[24] have been used in order to increase the yield of secondary ions per primary ion impact. By shining a highly energetic laser beam above the analysis sample neutrals can be ionised as they are sputtered from the surface. However the technique of sputtered neutral mass spectrometry (SNMS) has not widely been applied[10].

2.3.2 Modes of Analysis Primary Ion Source Operation.

Two modes of primary ion source operation have been used in this thesis for the analysis beam. These are the bunched mode which provides high mass resolution at the expense of the spatial resolution and burst alignment mode whereby the opposite is true. In order to have high mass resolution the pulse width must be narrow, producing a short stream of primary ions which impact the sample in quick succession. By pulsing the primary ion gun for <20 ns, a beam within the primary ion column physically measuring mm in length is produced. In order to artificially further reduce the effective pulse width a buncher is used in the bunched mode. This acts to provide kinetic energy to the ions following the first one so that the pulse of ions will impact the sample surface a known distance away at approximately the same time. This increases the energy deposition rate of the primary ion impact at the surface. This produces high secondary ion counts and reduces the time taken for secondary ion generation and extraction, improving the mass resolution[10]. However for imaging purposes the spatial resolution is diminished as the use of a buncher introduces an energy spread in the ions and chromatic aberrations in the lenses which degrades the beam size from being highly focussed to being defocused and broader[10]. As such high mass and spatial resolution is currently beyond the capabilities of modern primary ion sources.

Burst alignment mode has also been used in this thesis. Typically the pulse width is greater than that used with bunched mode, an 80 ns pulse width was used in the work shown in Chapter 5. A buncher is not used for burst alignment mode, as such a comparatively long stream of highly focussed primary ions impact the surface. The lack of use of a buncher and the long pulse width causes the mass resolution to suffer and secondary ion counts generated are also lower as impacts are less energetic. Due to the high focus of the primary ion beam the secondary ion images are well resolved with resolutions of 200 nm being routinely achieved[25]. Below, Figure 2.6 compares bunched mode and burst alignment mode showing the mass resolution obtained.

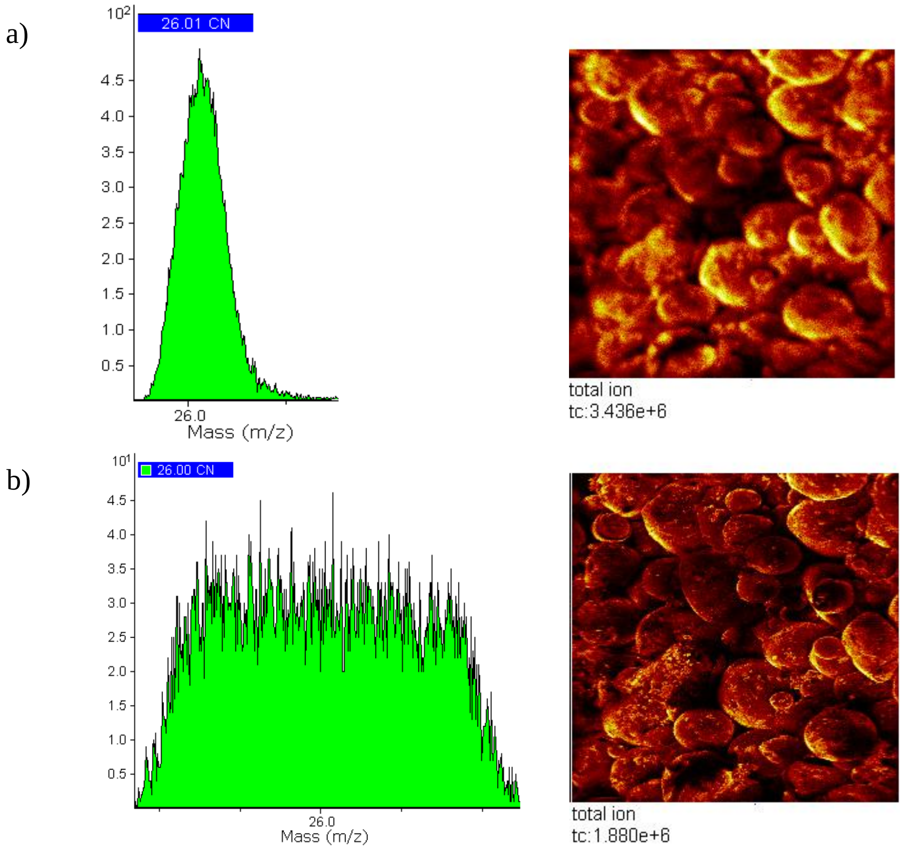

Figure 2.6 a) Shows a peak derived with the bunched mode of operation and b) shows burst alignment, for the CN^- ion in the negative spectrum for a microsphere system. Corresponding total ion images from each scan are also displayed from a 500 µm^2 area taken at 256 × 256 pixel resolution raster.

As the bunched mode of operation indicates there are no peaks within 1 mass unit either side of *m/z* 26 this peak can be used for analysis with burst alignment mode. From the ion images displayed the resolution is clearly greater for the bunched mode however, the total ion counts is also shown to be approximately half that achieved with bunched mode shown in Figure 2.6a.

2.3.3 Charge Compensation

Charge compensation is a fundamental aspect of ToF-SIMS devices for the analysis of the neutral organic materials studied in this thesis. Due to the bombardment of the surface with positively charged ions the surface potential increases caused by this input of positive ions and extraction of secondary electrons. If the charging is unimpeded it can cause positive ions to be accelerated through repulsion from the surface at kinetic energies beyond the acceptance window of the analyser resulting in the loss of the spectral data[26]. This build up of charge is countered in this thesis with the use of an electron flood gun which irradiates the surface with low energy electrons. These electrons are attracted to areas of high positive charge in an attempt to neutralise the surface charge. A limitation of the flood gun is that it has been shown to degrade the sample surface[27], as such in line with recommendations of the literature[27, 28] the electron dose was kept below 6.3×10^{18} electrons m^{-2}.

2.3.4 Example ToF-SIMS Surface Spectrum

Figure 2.7 below shows the example positive spectrum of the polyester, poly(l-lactic acid) (PLA).

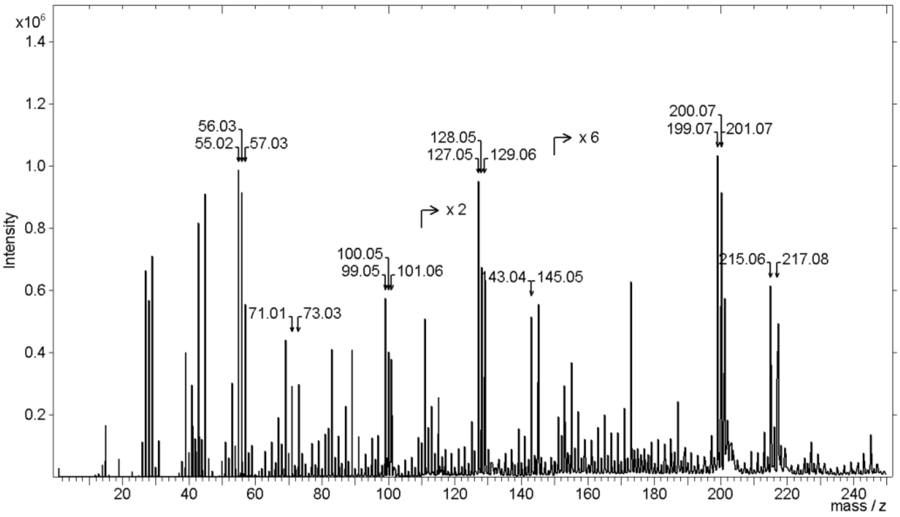

Calculated Characteristic Ions of PLA ($C_3H_4O_2$)	**Calculated Mass (*m/z*)**
[M - OH]$^{+}$	55.02
[M - O]$^{\bullet+}$	56.03
[MH - O]$^{+}$	57.03
[M - H]$^{+}$	71.01
[M + H]$^{+}$	73.03
[2M - CO2 - H]$^{+}$	99.05
[2M - CO2]$^{\bullet+}$	100.05
[2M - CO2 + H]$^{+}$	101.06
[2M - OH]$^{+}$	127.04
[2M - O]$^{\bullet+}$	128.05
[2M + H - O]$^{+}$	129.06
[2M - H]$^{+}$	143.03
[2M + H]$^{+}$	145.05
[3M -OH]$^{+}$	199.06
[3M - O]$^{\bullet+}$	200.07
[3M + H - O]$^{+}$	201.08
[3M - H]$^{+}$	215.06
[3M + H]$^{+}$	217.07

Figure 2.7 Positive ToF-SIMS spectrum of a thin film of PLA with characteristic ions tabulated. **M** represents the repeating unit of PLA ($C_3H_4O_2$), the mass has been calculated based on the sum of the precise mass of each element (to 2 d.p.).

The spectrum presented is in agreement with that originally reported by Davies *et al*. 1989[29] however improvements in cluster primary ion sources (explained in section 2.3.5) have increased the secondary ion counts by two orders of magnitude. A greater yield of high molecular weight fragments is also observed, because less fragmentation of the surface chemistry occurs when bombarding with large clusters of ions when compared with small high energy primary ions. SIMS is also capable of showing great intensity highly unstable radical cations such as $[\mathbf{M - O}]^{\bullet +}$. These odd numbered ions allow for qualitative identification of the sample being analysed and further confirmation of the origin of the surrounding even ions in unknown samples. Intense peaks which are not described in Figure 2.7 are important in furthering our understanding of end group effects and variability in fragmentation pathways[29] in addition to highlighting any contaminants in the spectrum.

2.3.5 Depth Profiling

Depth profiling of organic material is undertaken in dynamic SIMS (DSIMS) mode which in this work used two individual ion beams mounted at 180º to one another. A dose of primary ions in excess of the static limit is rastered across the analysis surface in order to form a precise flat bottomed crater within the analyte, exposing a section of the bulk available for undegraded analysis[10]. This is achieved by either using large clusters of ions which impact in quick succession or by using large primary ions such as buckminsterfullerenes. By using large ions or clusters, the energy spread of the impact is increased reducing the energy deposition rate of ion impact (as the energy is spread across multiple atoms). Secondary ions are generated from within the crater producing a spectrum derived from depths which are still representative of the original chemistry but at a greater depth than those possible with S-SIMS[10] shown in Figure 2.8.

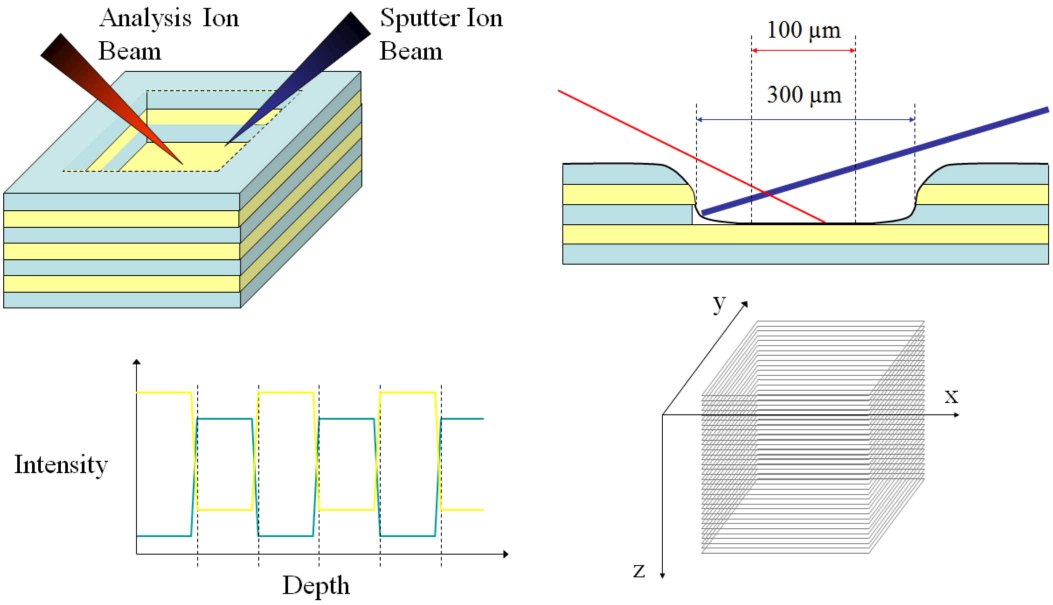

Figure 2.8 Schematic diagram of dual beam depth profiling. Adapted from IONTOF ©.

Depth profiling can be undertaken using two methods, a sequential application of the sputter beam followed by the application of the analysis beam generating data points at intervals. Using this regime the two primary ion beams are not active at the same time. The sputter source would remove some material, typically for some time, after which the crater would be analysed. This reduces the duty time for the sputter beam causing a corresponding increase in the measurement time. Alternatively interlaced mode can be used whereby both beams are active at the same time with sputtering and analysis taking place quasi-continuously. Interlaced mode improves the depth resolution observed. Data are acquired in automated µs cycles presented in Figure 2.9 as opposed to adhering to lengthy cycles of sputtering and analysis. Depending on the length of the sputter cycles, data can be lost, diminishing the depth resolution. Interlaced mode was used for analysis throughout the presented work.

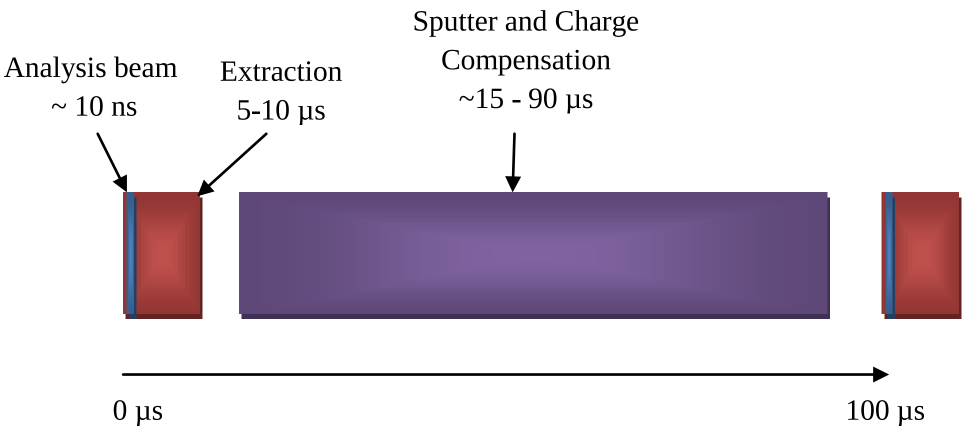

Figure 2.9 Schematic of the timing used in interlaced mode showing one cycle of sputtering and analysis. Adapted from Iltgen *et al.*[30]

The MD image shown below (Figure 2.10) illustrates the improvement from using larger primary ions for sputtering. There is an increase in sputter yields and energy deposition occurs at the outer surface spread across multiple primary ions/atoms rather than penetrating the analyte, common for monatomic primary ions where all the energy impacts with the single ion[15, 31]. These advances allow for accurate molecular depth profiling. Examples of primary ion beams used for a cluster ion source are C_{60}^+ [32, 33], Bi_n^+ [34], Au_n^+ [35] and SF_5 [36, 37], each exhibiting diverse characteristics. These characteristics are related to charge and metallic or non-metallic chemistry, however, they all show a net increase in secondary ion fragment size and sputter yield when compared with monatomic primary ions and lead to a reduction in ion beam induced damage[31]. Mass is the key contributor to sputtering rate, thus a large primary ion will cause less fragmentation due to having a softer ionisation regime unlike grouped impacts of numerous small primary ions which leads to a higher energy deposition at the surface[10]. This causes more fragmentation and therefore smaller less distinct *m/z* fragments being evoked[38].

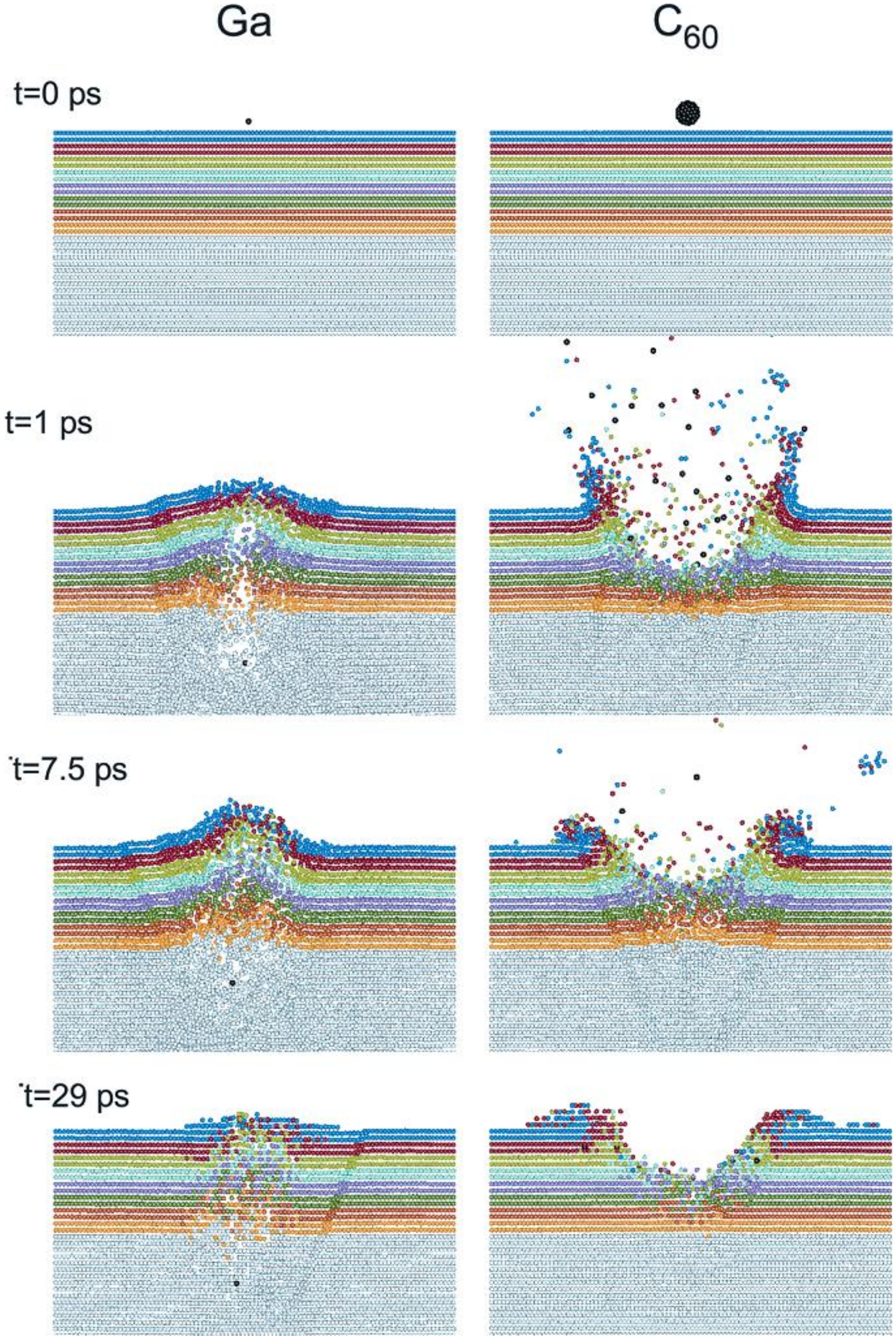

Figure 2.10 Schematic diagram of damage caused to a gold substrate by Ga, and C_{60} primary ion sources, also indicating difference in sputter yield and sub-surface damage[15].

The damaging effect of bismuth primary ions used for analysis has also been investigated[39]. The effect of the analysis beam in dual beam depth profiling has largely been neglected however it has been shown high bismuth primary ion doses can contribute to deterioration in the interface widths in an organic polymer – inorganic substrate model. Furthermore it has been postulated that increasing the number of interfaces, for instance through casting multiple layers the effect of the analysis beam may be exacerbated[39].

For depth profiling ~200 pA target current was used for C_{60}^+ organic depth profiling in this thesis which is congruent with recommendations from the literature[40]. The bismuth source with a 25 keV impact energy used in throughout this thesis was operated with a target current maintained at ~1 pA with a pulse width of 10.5 ns was adhered to in order to improve mass resolution, reduce the observation of detector saturation and non-linearity of the intensity scale.

Improvement in molecular ion yield of 3 to 4 orders of magnitude from using C_{60}^+ for analysis compared with established monatomic Ga^+ ions[41]. This is coupled with a tendency for the use of high primary ion current to maximise detection sensitivity for low intensity ions. Detector linearity is therefore an area of increasing importance[42]. Linearity of the intensity scale is crucial for interpretation of the data and subsequent analysis with techniques such as multivariate analysis, (described in section 2.5) or isotopic ratio measurements[43]. Non-linearity of the intensity scale is caused by detector saturation, where secondary ion counts are too intense for the detector to sufficiently characterise all ions that impact it, affecting the reproducibility of the data collected. In order to reduce such non-linearity issues, dead time correction was used. For high-intensity mass peaks automated dead time correction which is a function of the IonSpec 4.5.0.0 software used in this work (ION-TOF GmbH, Münster, Germany) can reduce the effect of detector saturation in order to maintain a linear intensity scale. This uses Poisson statistics in order to correct for the fact only one secondary ion per nominal mass can be detected for each primary ion pulse[44, 45].

2.3.6 ToF-SIMS Instrumentation

A ToF-SIMS IV[46] (ION-TOF, Münster, Germany) retrofitted with a bismuth and C_{60} columns was used for all SIMS data shown in this thesis. An automated electronic stage control module was used to move the stage within the main chamber. The pressure was maintained below 6×10^{-8} Torr for analysis but within the initial load lock a pressure of 1×10^{-6} was sufficient to move the sample stage from the load lock to the main chamber. When loading the sample stage into the ToF-SIMS anti-static gloves were used in order to reduce the opportunity for any static charge to influence electronics within the main chamber.

2.4 X-ray Photoelectron Spectroscopy

X-ray photoelectron spectroscopy (XPS), also known as electron spectroscopy for chemical analysis (ESCA) is a UHV technique capable of generating quantitative information from its analysis depth of between 5 and 10 nm. It measures the elemental composition and chemical state of the analyte. The analysis is limited to atoms of a mass above 3; as such it is unable to discern hydrogen and helium.

In this thesis, high energy aluminium X-rays (1486.6 eV) were used to irradiate the sample in order to cause the excitation of electrons evolved from the top 5 - 10 nm of the surface, which are termed photoelectrons. The photoelectrons are emitted after a transfer of energy from a photon (X-ray) to the core-level electron, which is termed the photoelectric affect (Figure 2.12a). These data can be used to identify the atomic and molecular environment that the detected electrons were in prior to being released from the sample which is expressed as the binding energy of the electron[10]. A spectrum is then plotted with the intensity of electrons detected as a function of binding energy. Although the X-rays themselves can penetrate deeper than 10 nm, photoelectrons emitted lose their energy during collisions and do not reach the detector. Electrons that lose some energy but still have enough to reach the detector are seen as background noise in the XPS spectrum[47]. Electrons that are emitted without any energy loss feature as characteristic peaks in the spectrum. The binding energy of electrons from all atoms in their original states is known as the initial state. Once chemical bonds are formed between atoms, a shift in the binding energy from the reference value indicates the covalent or ionic bonding between atoms and allows for identification and quantification[10, 48]. The intensity of the peaks at the various binding energies can be used to directly quantify the chemical composition of the sample as intensity is directly proportional to the concentration of the atom within the sample[48, 49].

Example XPS data for PLA is shown in Figure 2.11 below. A survey scan of a spectrum of PLA and a high resolution scan of the C1s orbital are shown.

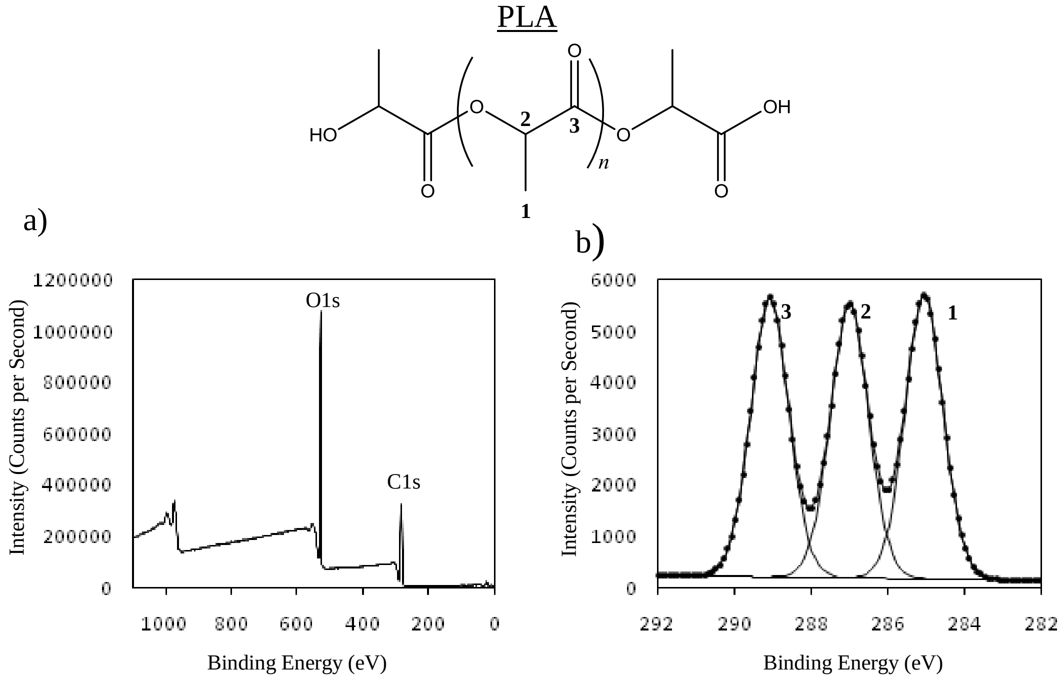

Element	**C**	**O**
% Composition	60	40

C1s	**C-C/ C-H 1**	**C-O 2**	**C(=O)-O 3**
E_B Shift (eV)	285	286.99	289.01
Area (%)	33.91	32.73	33.36
Calculated (%)	33	33	33

Figure 2.11 a) A survey scan and b) a high resolution scan of pure PLA, the numbering on the PLA structure locates the 3 carbon atoms in each repeating unit.

While the area under the C1s peak and intensity in Figure 2.11a is lower than that of the O1s electrons, the atomic composition is greater for carbon. This is due to the use of relative sensitivity factors (RSF), used to scale the measured peak intensity to account for the fact certain elements emit electrons easier than others, normalising the ion counts by empirically derived RSFs. For the work in this thesis, RSF values provided by the instrument manufacturer were used for all analysis to allow for accurate quantification.

When a photon collides with an atom one of three outcomes is possible:

- Photon can pass through.
- Photon can be scattered by an orbital electron leading to partial energy loss (inelastic scattering).
- Photon transfers all energy to an orbital electron leading to electron emission, providing the energy is higher than its threshold limit (Figure 2.12a).

A schematic of the scenario described in the third bullet point is shown in Figure 2.12a. A schematic for a typical XPS instrument shown in Figure 2.12b and a schematic for the array of delay-line anodes used for detection of the electrons is shown in Figure 2.12c.

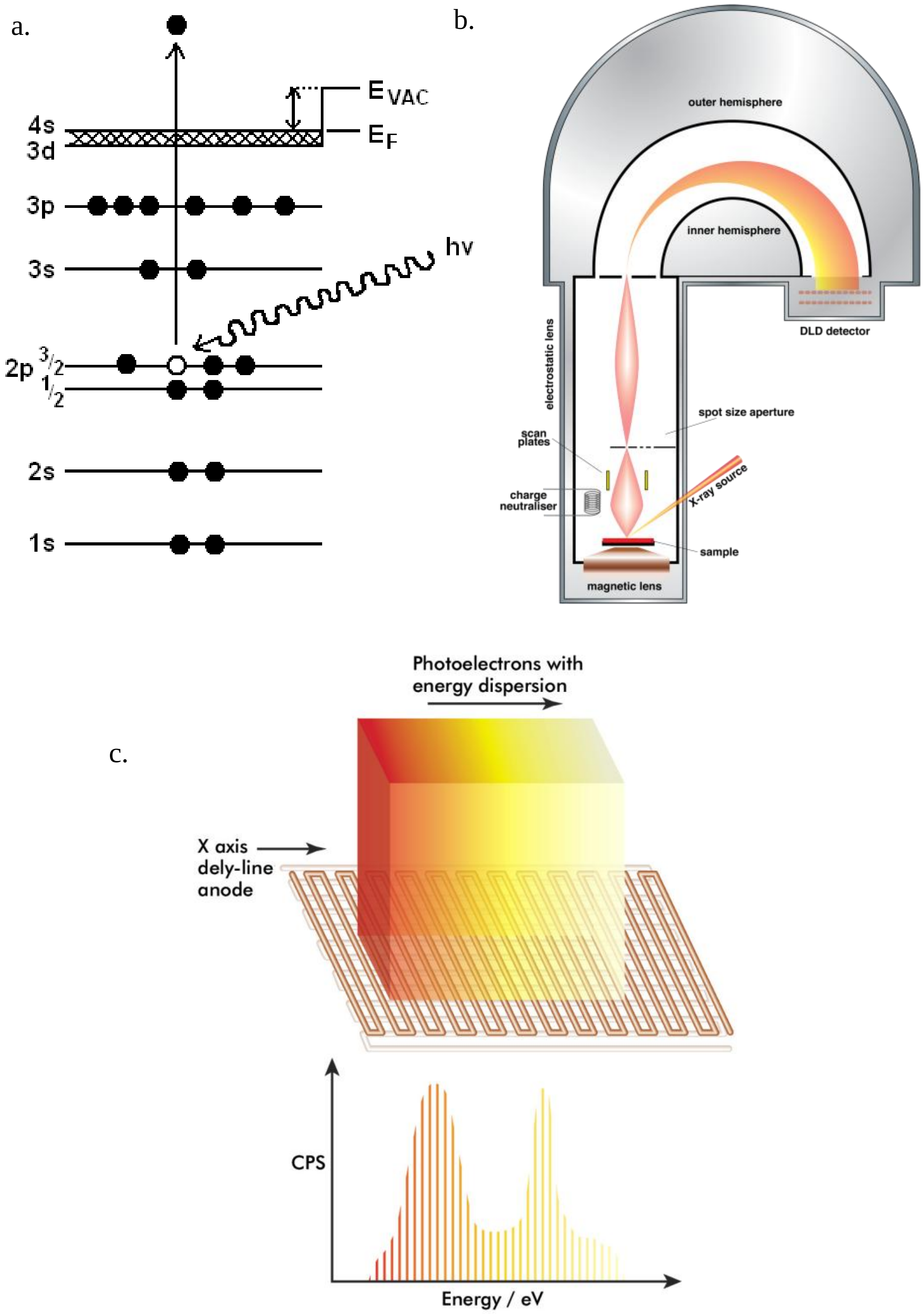

Figure 2.12 a) Schematic illustration of photoelectrons being released from the core level[10]. b) Schematic of an XPS spectrometer (Axis Ultra with delay-line detector) Kratos Analytical, Manchester©. c) Schematic of electron detection after hemispherical separation reproduced from Kratos Analytical, Manchester©.

The components required for an XPS instrument include the vacuum system, X-ray source and an electron energy detector. Similar to ToF-SIMS the vacuum system is vital as the electrons in this instance must be able to reach the detector without collisions with gas phase molecules and for optimal X-ray source operation. While XPS is not as surface sensitive as ToF-SIMS, it is important to reduce any sources of contamination of the analysis sample which is aided by the use of a vacuum system. The X-ray beam is produced by applying a 10 keV electron beam to a target anode (in this case aluminium) which in turn emits fluorescence X-rays and electrons. This beam then travels through an X-ray monochromator in order to purify the beam so that any electrons, satellite X-rays or heat radiation will not be transmitted onto the sample[10]. This is important as the addition of 'impurities' to the X-ray beam may lead to sample degradation, and the increase in background noise through inelastic scattering.

The detector comprises of a collection lens, an energy analyser and the detector. Once the electrons have been emitted from the surface they travel through the extraction optics via an aperture, used in order to improve the depth resolution[50]. The electrons then pass through an electrostatic hemispherical analyser (shown at the top of Figure 2.12b) which consists of two concentric hemispheres with a potential difference across them so the outer hemisphere is negative and the inner is positive with respect to the potential at the center line (known as the pass energy). Deflecting electrons and separating them based on their electronegativity[51]. In this thesis a delay line detector was used. This analyser uses a multi-channel plate stack[52] above an array of equally spaced delay-line anodes (allowing for detection of location/timing of particle impacts), associated control units convert a charge pulse on the delay-line anodes to a digital signal which is further processed to generate spectra or images. The kinetic energy of emitted electrons is related to the frequency of the exciting photons[48]. The following equation (Equation 2.2) can be used to discern the binding energy of the electron in the atom.

$$E_B = h\nu - KE$$ **Equation 2.2**

Where E_B is the binding energy of the electron in the atom, $h\nu$ is the energy of the X-ray source and KE is the kinetic energy of the emitted electron.

The measurement of electron binding energy allows the identification of the element and its chemical state[48, 49]. Less energy is required to collect photoelectrons in the electron shells furthest from the nucleus than for those levels close to the positively charged nucleus[10]. Binding energies are higher in layers closer to the nucleus due to electrostatic attraction[10]. As the binding energies and chemical shifts have been previously referenced, the spectra can be compared with such reference sources as 'The Scienta ESCA300 Database' by Beamson and Briggs[53] to determine the elements and chemical environment of the detected electrons.

In order to improve the attainable depth resolution, sample stage rotation can be used in order to use a grazing angle of incidence of ~ 15°. By reducing the incident beam angle, the depth from which the XPS information is obtained is reduced. The inelastic mean free path (IMFP) of emitted electrons from the sample is a measurement of how far an electron can travel through a solid before losing energy[10]. Changing the take-off angle from 90° to 15° causes a ~73% improvement in the surface specificity of the data generated however a decline is noted in the electron yield[10]. Typically many commonly used detectors are unable to measure electrons from an angle < 20°[10, 48, 49].

Similar to ToF-SIMS, XPS instruments can have sputtering sources affixed in order to depth profile organic materials[54-56]. However this is a recent development with respects to organic material as prior to 2007, XPS devices were only commonly equipped with argon etching sources, suitable for depth profiling inorganic material. These cause too much damage to organics to provide useful data[57].

2.4.1 XPS Instrumentation

In this thesis a Kratos Axis Ultra (Kratos, Manchester, UK) XPS instrument was used exclusively. Aluminium X-rays were used at a power of 450 W with a pass energy of 80 eV for the C1s, O1s and N1s depth profiles. Survey scans were taken routinely from the spectral range of 0 - 1100 eV at a pass energy of 160 eV. The higher the pass energy the lower the resolution of the spectrum but greater the intensity obtained making higher pass energies suitable for survey scans[10].

2.5 Multivariate Analysis for De-convolution of Data.

SIMS is generally viewed as a qualititative technique, due to the matrix effects on ion yields described in section 2.3.2. Therefore the intensities seen in SIMS experimentation may not be an entirely accurate method of measuring the concentration of the ions in the sample. This is in contrast with XPS in which the area under the graph can be used to establish the relative concentrations of certain groups[58]. The matrix effect however is seen to be minimal in most organic biomaterial and polymeric films[18].

As each pixel in a ToF-SIMS image comprises one mass spectrum, multivariate analysis is a technique used to de-convolute the hyperspectral data generated. The ToF-SIMS instrument is capable of rastering a sample area taking numerous scans; in this case each pixel contains the sum of each spectrum from each scan. Tyler *et al*. 2007 have shown principal component analysis (PCA) and maximum autocorrelation factors (MAF) analysis of four SIMS images to demonstrate the de-convolution of SIMS images possible[59]. Additional forms of multivariate analysis include; multivariate curve resolution (MCR)[60], neuronal networks (NN) and mixture models (MM)[61].

PCA is able to reduce the size of large data sets with a minimal loss of information. This is achieved by identifying the variance in a data set and reducing its dimensionality by comparing peaks across a number of spectra and calculating new variables termed ‘principal components'[61]. PCA therefore reduces the amount of data by taking into account the variables that account for the majority of the variation seen across the different spectra[62].

MCR has been shown to be a valuable technique for analysis of samples with considerable topography and those which contain numerous components to differentiate[60]. As shown in Figure 2.13b MCR factors extract what is modelled to be the most divergent data in an effort to extract pure components from a mixed system. MCR has non-negativity constraints and will fit the number of principal components to the number requested, unlike PCA which will only yield useful results if above 95% of the variance in the data is accounted for. MCR is used to extract pure components from a multi-component analysis, fulfilling the role of multivariate analysis to de-convolute data. PCA and MCR are described graphically in Figure 2.13.

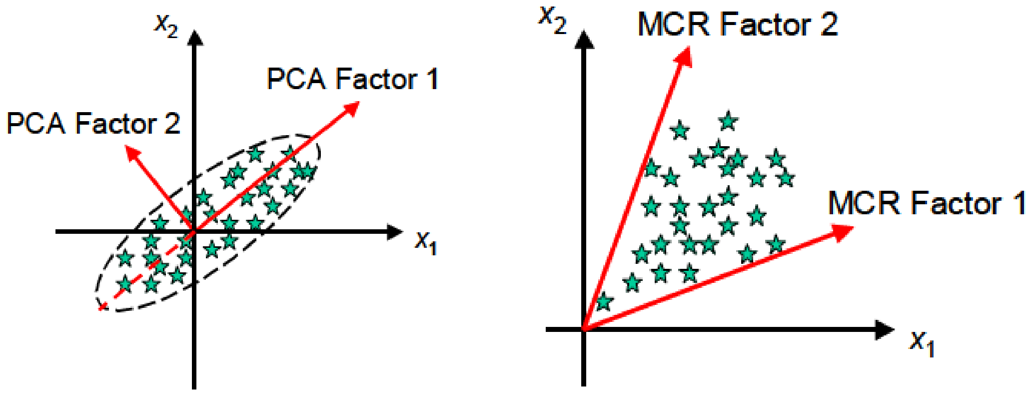

Figure 2.13 a) PCA and b) MCR modelling described graphically[63].

A limitation of PCA is that low intensity secondary ions from larger molecules of interest may be lost in the processing due to the pre-processing. Before being run through the PCA process the data is prepared (normalisation/mean centering etc.) so the onus is still on the analyst to recognise certain important peaks and pre-process the data accordingly[59, 62]. Multivariate analysis therefore is a vital tool to describe the spectral data produced however the analysts experience is still important in the interpretation of ToF-SIMS data.

2.6 Spectroscopic Ellipsometry

Ellipsometry is an optical measurement technique that is able to discern the optical properties of thin films on reflective substrates. A standard ellipsometer (represented in Figure 2.14) measures the change in polarised light upon reflection from a sample[64]. Light polarisation is expressed as Ψ and Δ which represent the changes in amplitude and phase of light respectively. When a wave enters a different phase, such as a thin film, electrons associated in the atoms of that phase oscillate at the frequency of the wave which slows the wave[64]. In addition energy from the wave can be transferred to the electrons which reduces the amplitude of the wave[64]. These processes determine the complex refractive index and can affect the change in light polarisation detected in ellipsometry. The change in polarisation on reflection is due to the sample's thickness and dielectric function in addition to the complex refractive index. Two types of polarisation exist that are orthogonal within polarised light. These are denoted parallel (*p*) and perpendicular (*s*)[64]. The ratio of the *p*-polarised to *s*-polarised components is termed the polarisation state. By measuring the polarisation state before and after the beam travels though the sample for analysis ellipsometry can probe the morphology, crystal quality, chemical composition or electrical conductivity of the thin films being analysed[64].

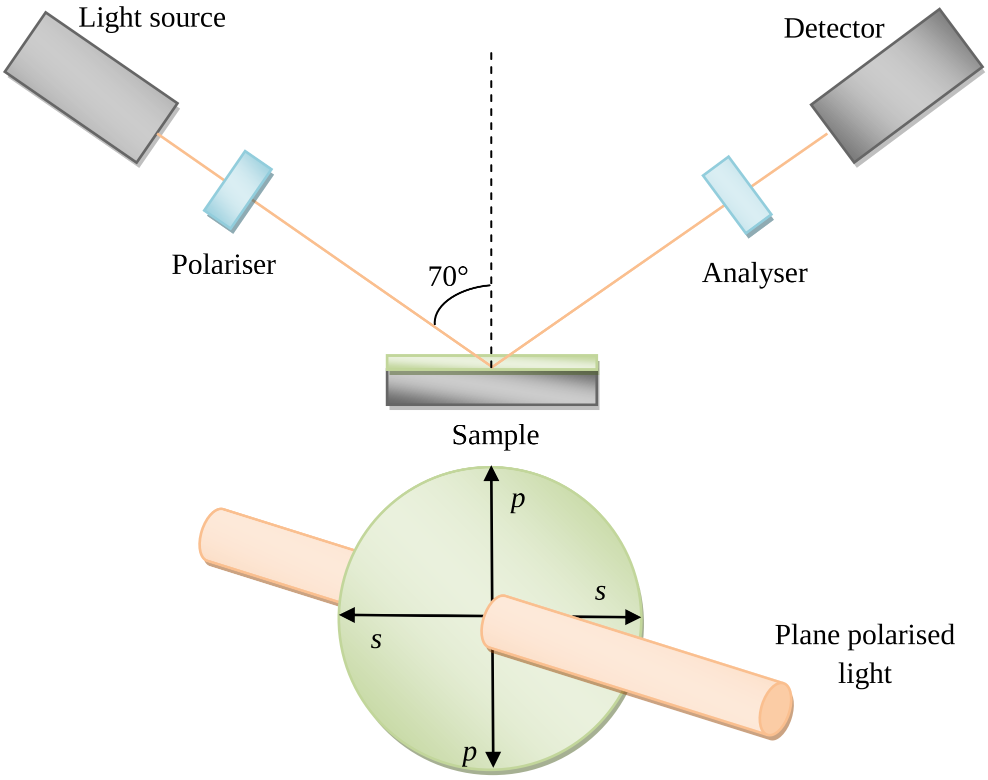

Figure 2.14 a) Schematic diagram of an ellipsometer, b) a schematic diagram of the polarisation of light that is compared before and after travelling through the film.

Ellipsometry is a highly precise technique with extremely high thickness sensitivity (~0.1 Å) due to the fact it relies on the polarisation state of light as opposed to other optical techniques that are limited by the diffraction of light. This precision however is limited by the diameter of the beam which is often ~3 mm, reducing the lateral resolution attainable. The wide beam diameter in the ellipsometry measurements is also impacted by the second limitation, surface topography and roughness. Non-uniformity in the surface topography will render the data generated unreliable as the diffraction of the plane polarised light will come from multiple thicknesses at the surface. Surface roughness can scatter the incident light considerably reducing the reflected light intensity, increasing errors[64]. Hence, in this thesis samples analysed with ellipsometry were fabricated in order to ensure they were as flat and uniform as possible which was confirmed with AFM analysis which will be discussed in section 2.8. Biomaterial research has utilised the refined method of ellipsometry since Langmuir and Shaefer showed in 1937 that light interference can be used to measure surface adsorbed antigen and the antibody attachment thickness[65]. Due to the capabilities of being able to determine the total amount of protein in an adsorbed layer without destruction or labelling of the protein it is a popular technique in this field[66-69] in addition to its routine use for the analysis of thin films.

In this thesis two ellipsometers were used, an alpha-SE and a M – 2000DI both manufactured by ellipsometer (J. A. Woollam Co., Inc., Lincoln, NE). For the samples analysed in this thesis the only tangible difference in the two instruments is that the M-2000DI routinely scans a spectral range from 193-1690 nm however the alpha-SE is capable of scanning from 380 - 900 nm. As such the spectroscopic and modelling accuracy of the M-2000DI is greater however the alpha-SE still provides highly accurate film thickness data.

2.7 Raman Microscopy

The Raman effect first described by Sir C.V. Raman in 1928[70]. It is widely used together with infra-red spectroscopy in the chemical and pharmaceutical industries in studying the vibrational and rotational modes in a system[71]. The Raman effect is caused by polarisation of the electron cloud surrounding chemical bonds when excited by an incident electromagnetic (EM) radiation[10]. This causes a vibration of the atoms within a bond. This vibration can be detected as the Raman effect causes scattering of the incident EM radiation which can be detected and used to form a spectrum[72]. Scattering of light after being exposed to a sample may be elastic or inelastic. The majority are elastically scattered and the process is termed Rayleigh scattering. Inelastic scattered photons are detected in Raman spectroscopy where the energy lost by photons is measured. Inelastic scattering of photons is generally a weak effect with ~ 1 in 10^{11} photons being inelastically scattered[10] which is termed Raman scattering. This type of scattering is encouraged with the use of a monochromatic high intensity laser. Inelastic scattering originates when photons from the incident light deviate from their original angle and plane of incidence. This phenomenon occurs after photons excite a molecule from the ground state to a virtual energy state. As the molecule leaves this virtual energy state, a photon is emitted and the molecule returns to a different vibrational state. If the final state is more energetic than the initial state, the emitted photon will have a lower frequency to balance the total energy of the system according to the law of conservation of energy[10]. This effect on the emitted photon is termed the Stokes shift. If the opposite is true the emitted photon has a higher frequency and is termed an Anti-Stokes shift[72] shown in Figure 2.15.

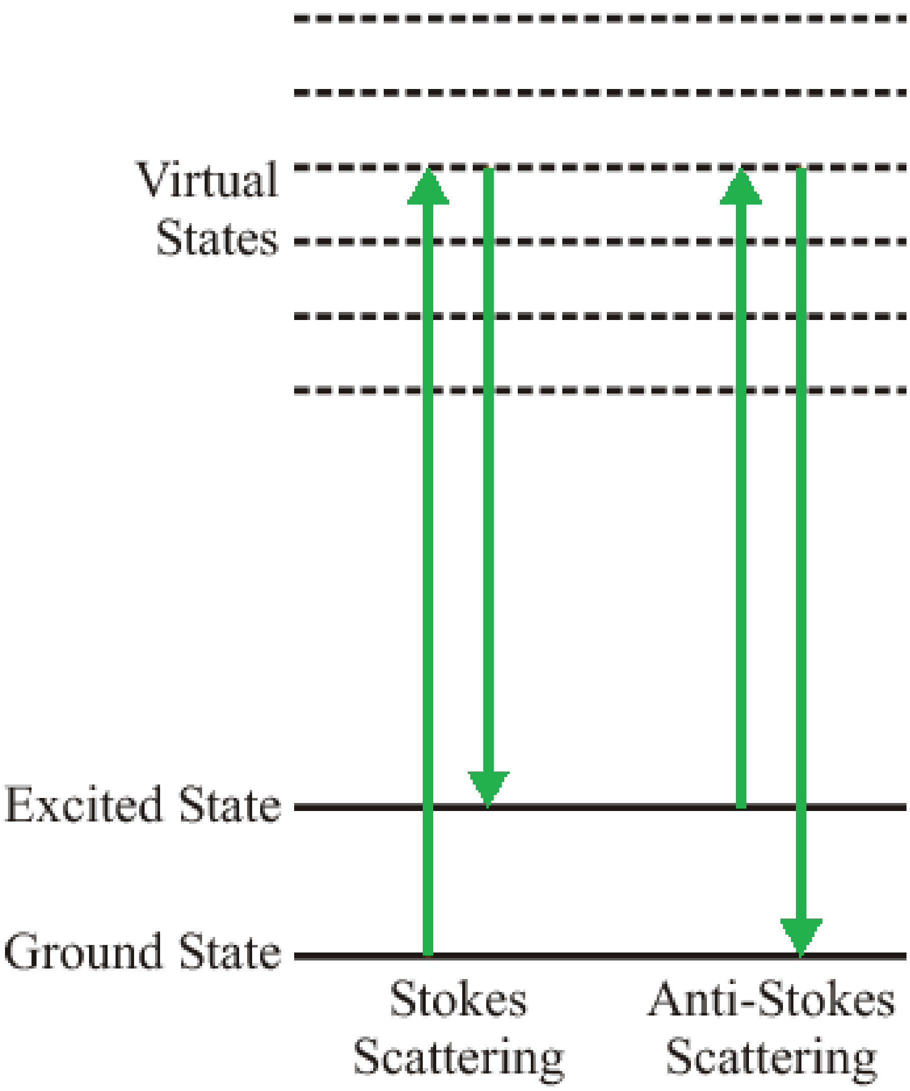

Figure 2.15 Schematic of Stokes and Anti-Stokes scattering.

The molecular vibrations which are detected create the Raman spectrum where intensity is plotted against the shift in the energy of the photons from the monochromatic laser. The Raman shift, measured in wavenumber, is well established and so the surface chemical composition can be derived[71]. The Raman spectra generated provides detailed, quantitative data allowing for the identification and differentiation of samples at ambient conditions without the need for complicated sample preparation as shown in Figure 2.16. Identification is made possible as the bond stretching bands, measured in wavenumber, are well characterised and therefore can be identified in a Raman spectrum. The area under the peaks can also be integrated in order to quantify the vibrational bond stretching bands highlighted in the Raman spectra for quantitative analysis[73, 74].

Figure 2.16 shows an example of Raman data used for differentiating four ring structured drugs, through their vibrational spectrum.

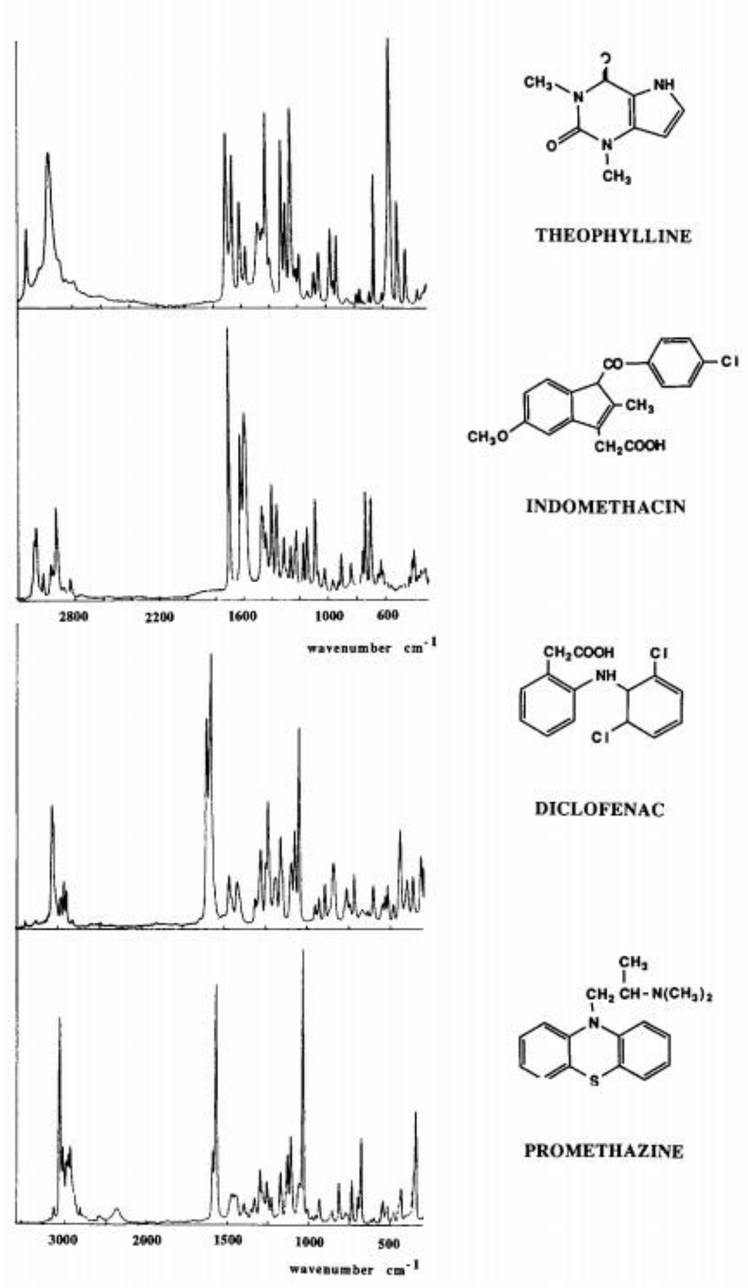

Figure 2.16 Example Raman spectra plotting intensity vs. wavenumber for four drugs[73].

In addition to the surface chemical properties, Raman spectroscopy can operate in confocal mode whereby point illumination is used to focus on an area within a transparent sample[75]. Only photons emitted from within ~1 µm of the focal plane are detected. This allows for non-destructive depth profiling of a specific plane within a sample providing complimentary non-destructive vibrational spectra complimentary to the more destructive ToF-SIMS and XPS depth profiling. The lateral resolution is affected by the spot size of the laser. The spot size will depend on the wavelength of the laser used due to the self-diffraction of light which leads to a beam diameter of fixed dimensions for a given wavelength to be emitted[10]. A green laser operating at 532 nm was used for the data presented in Chapter 5 as this provides the narrowest beam available and thus the highest spatial resolution.

In this thesis a WITec CRM 200 confocal Raman microscope (WITec, Ulm, Germany) was utilised with the WITec Project v1.92 software, a schematic of the instrument is displayed in Figure 2.17.

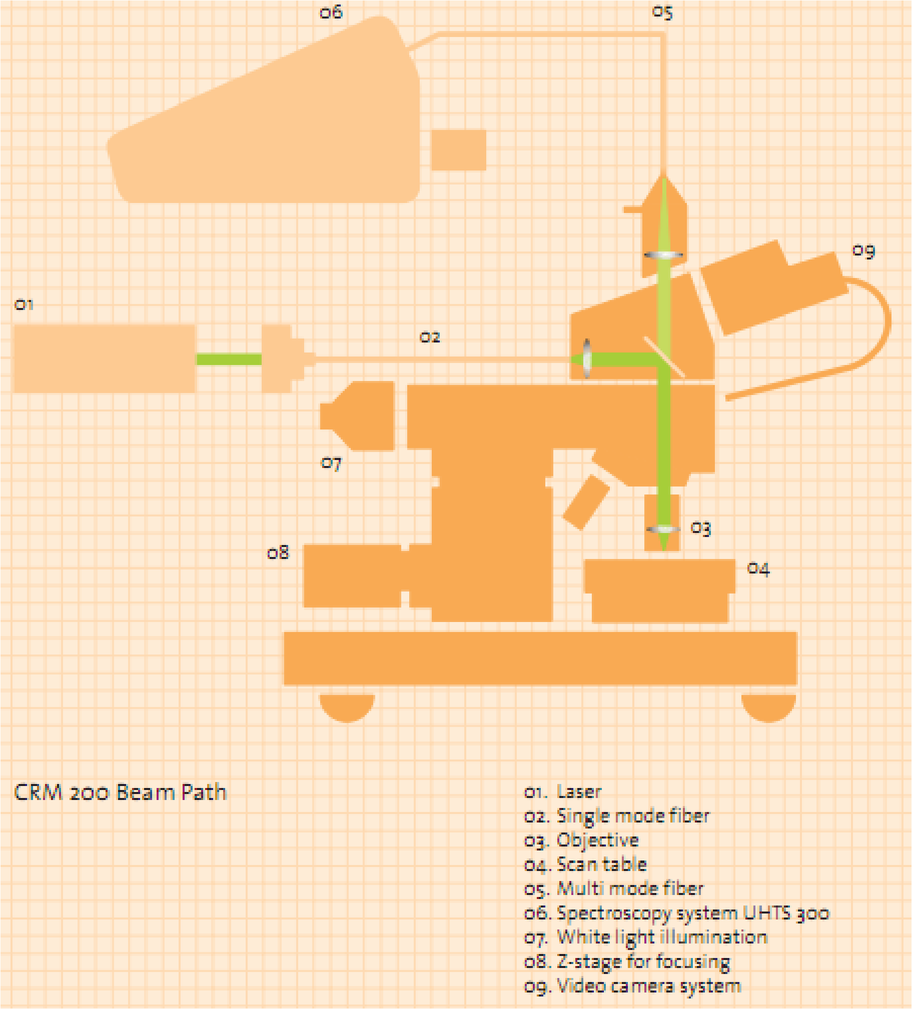

Figure 2.17 Raman instrument schematic (WITec CRM200, WITec Ulm, Germany).

The laser travels through a monochromator and focusing optics in order to purify the exciting beam. The monochromator transmits a narrow band of wavelengths of light from a wider range of wavelengths available, acting as a filter of wavelengths close to that of the exciting laser. This laser is shone on the sample surface which then reflects the laser light in a 180° backscattered regime back up the objective lens[76, 77]. A range of objective lenses can be attached in position 3 in order to alter the lateral resolution attainable by focussing the laser beam to a small spot size. However unlike ellipsometry, the lateral resolution of Raman analysis is limited by the diffraction of light (~200 nm)[78]. This scattered light travels through focusing optics and filters to maintain high signal and subtract Rayleigh scattered light and the contribution of the exciting laser itself which may affect the spectral resolution observed to a charged coupled device (CCD) detector. A CCD is a silicon based multichannel array which is sensitive to light making them suitable for acquisition of Raman spectra[79]. Multichannel arrays allow for an entire Raman spectrum in one acquisition. Within this array ~millions of detector elements known as pixels are present[79]. Each element is sensitive to light and builds a charge when exposed to light. The brighter and longer the duration of exposure the greater the electric charge which is converted into the spectra observed[79, 80]. The light is dispersed using a diffraction grating which works similar to a prism, separating the light into different wavelengths which is projected onto the CCD array. The first elements detect light from the low edge of the spectrum i.e. ultraviolet and through this mechanism a large band of wavelengths can be converted into a complete spectrum simultaneously[77].

Electron multiplying charged coupled devices (EMCCD) are another commonly used type of detector for Raman spectroscopy. This type of detector is often used for confocal Raman mapping where the signal is weak. In addition to a standard readout register there is also an electron multiplying (EM) register. This uses a higher voltage causing electrons to acquire sufficient energy that impact ionisation occurs[81]. Impact ionisation probability is low however as there are often hundreds of elements the gain can be high[81]. When ionisation occurs extra electrons are produced and stored in the next pixel. amplifying the signal encountered, drawing low intensity peaks out from the noise[81].

2.8 Atomic Force Microscopy

AFM is a scanning probe technique developed from scanning tunnelling microscopy developed in 1986[82] which is capable of resolving details down to 2 - 3 Å[83, 84]. A schematic of a typical AFM is shown in Figure 2.18 below.

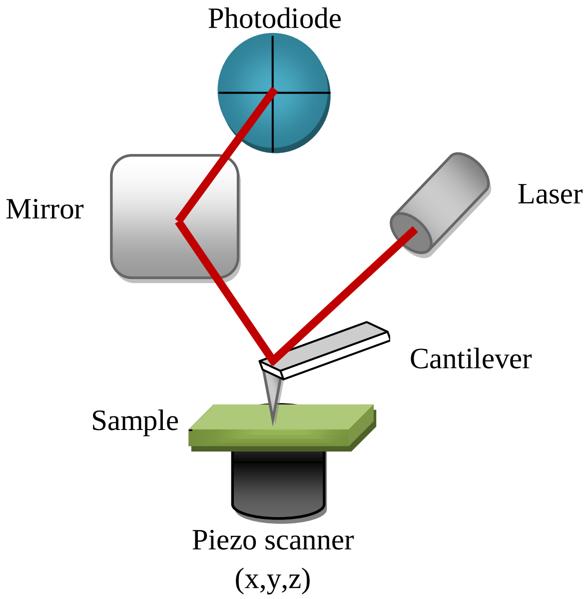

Figure 2.18 Schematic representation of a typical AFM.

AFM tracks the movement of a tip over a sample with feedback mechanisms allowing a piezo scanner to control the tip at a constant force above the surface[85-87]. Tip movement is monitored by the laser focussed above the cantilever tip which is in contact with the sample. The laser reflects off a mirror onto a photodiode the position of which is calibrated at rest to hit within the center of 4 photodiodes. As the probe scans the surface, any deflection of the sensitive cantilever causes corresponding movement of the laser which is detected by the photodiode. The signal from the photodiode can be converted into an accurate high resolution topographical image[85, 88]. The photodiode also has a feedback mechanism to control the piezo scanner facilitating the use of a range of modes.

AFM is capable of measuring adhesive and repulsive forces, through the measurement of both interaction and separation of the cantilever tip from the surface, force-distance curves can be acquired[84, 85, 89]. Intramolecular forces can be measured using force-distance curves, for polymers these forces result from the elasticity of the polymers as well as structural changes along the polymer chain[90]. The information generated by the force-distance curves can provide a wealth of information on the mechanical properties such as adhesion, elasticity, deformation and energy dissipation[91] as described in Chapter 1.

Three main modes of AFM operation exist, contact, non-contact and tapping modes. Contact mode is where the cantilever is kept in contact with the sample and is rastered over the sample either at a constant height (fixed z-axis) or at a constant force (dynamic z-axis). The constant contact allows for high resolution accurate topographical images to be produced however with soft materials such as thin polymer films contact mode, damage is likely to occur[84, 92]. Both non-contact and tapping mode overcome this disadvantage. Non-contact mode is where the tip is oscillated at its resonance frequency between 10 and 100 nm above the sample surface and attractive forces are measured by measuring the change in the oscillation[84]. The change in tip oscillation caused by the interaction forces between the sample and the tip allows for a form of chemical characterisation of the surface.

Regions of heterogeneous chemistry will have a different, quantifiable affect on the attraction of the cantilever. This can be mapped and is termed phase imaging. Tapping mode combines the advantages of both modes without the inherent disadvantages of contact mode and thus is the basis for all AFM analysis in this thesis. In tapping mode the cantilever is oscillated at a high frequency with the amplitude kept constant. The tip comes into contact with the surface of the sample, however it is not scanned while in contact and so reduces the damage from the sharp tip making it suitable for the analysis of soft polymers.

A recently developed mode termed quantitative nano-mechanical or QnM mode has been developed which operates in tapping mode. This mode is able to acquire force-distance curves for each pixel in an acquired topographical image. While this limits the scan speed, increasing the acquisition time it is able to provide information as to the Young's modulus and adhesion in addition to the data acquired in traditional tapping mode alone[84, 85, 93]

2.8.1 AFM Instrumentation

In this thesis a Veeco MultiMode AFM scanning probe microscope was used (Veeco, Santa Barbara, CA, USA) for analysis using tapping mode in air, 10 × 10 µm areas were analysed for the work in Chapters 3 and 5. Bruker RTESPA silicon nitride probes (Bruker, Billerica, MA, USA) were the cantilevers selected. They are the most commonly used tips for tapping mode in air due to the rotated tip which provides a more symmetrical representation of features greater than 200 nm.

2.9 References

1. Morinville, W., C. Krasinski, and Ieee, *Secondary ion mass spectrometry analysis of wafer contamination resulting from gloved hands*. 2006 IEEE Workshop on Microelectronics and Electron Devices. 2006, New York: Ieee. 35-36.
2. Oran, U., E. Ünveren, T. Wirth, and W.E.S. Unger, *Applied Surface Science*, 2004. **227**(1-4): p. 318-324.
3. Vickerman, J.C. and D. Briggs, *ToF-SIMS: Surface Analysis by Mass Spectrometry*. 2001, Manchester: Surface Spectra Ltd.
4. Green, F.M., I.S. Gilmore, and M.P. Seah, *Rapid Communications in Mass Spectrometry*, 2008. **22**(24): p. 4178-4182.
5. Shard, A.G., F.M. Green, P.J. Brewer, M.P. Seah, and I.S. Gilmore, *Journal of Physical Chemistry B*, 2008. **112**(9): p. 2596-2605.
6. Kern, W., *Handbook of Semiconductor Wafer Cleaning Technology*, ed. W. Kern. 1993, New Jersey: Noyes Publications.
7. Ogaki, R., F. Green, S. Li, M. Vert, M.R. Alexander, I.S. Gilmore, and M.C. Davies, *Applied Surface Science*, 2006. **252**(19): p. 6797-6800.
8. Shard, A.G., M.C. Davies, S.J.B. Tendler, D.E. Jackson, P.N. Lan, E. Schacht, and M.D. Purbrick, *Polymer*, 1995. **36**(4): p. 775-779.
9. Gesang, T., W. Possart, O.D. Hennemann, and J. Petermann, *Langmuir*, 1996. **12**(13): p. 3341-3350.
10. Vickerman, J.C. and I.S. Gilmore, *Surface Analysis: The Principal Techniques*. Vol. 2. 2009: John Wiley & Sons Ltd.
11. Delcorte, A., *Nuclear Instruments and Methods in Physics Research B*, 2005. **236**: p. 1-10.
12. Delcorte, A. and P. Bertrand, *Nuclear Instruments and Methods in Physics Research B*, 1996. **115**: p. 246-250.
13. Delcorte, A., P. Bertrand, and B.J. Garrison, *Journal of Physical Chemistry B*, 2001. **105**(39): p. 9474-9486.
14. Krantzman, K.D., Z. Postawa, B.J. Garrison, N. Winograd, S.J. Stuart, and J.A. Harrison, *Nuclear Instruments and Methods in Physics Research B*, 2001. **180**: p. 159-163.
15. Postawa, Z., B. Czerwinski, N. Winograd, and B.J. Garrison, *Journal of Physical Chemistry B*, 2005. **109**(24): p. 11973-11979.
16. Wagner, M.S. and D.G. Castner, *Langmuir*, 2001. **17**(15): p. 4649-4660.
17. Bertrand, P., *Applied Surface Science*, 2006. **252**(19): p. 6986-6991.
18. Belu, A.M., D.J. Graham, and D.G. Castner, *Biomaterials*, 2003. **24**(21): p. 3635-3653.
19. Herzog, R.F.K. and F. Viehboeck, *Physical Review*, 1949. **76**: p. 855 - 856.
20. Liebl, H.J. and R.F.K. Herzog, *Journal of Applied Physics*, 1963. **34**(9): p. 2893-&.
21. Castaing, R. and G. Slodzian, *Comptes Rendus Hebdomadaires Des Seances De L Academie Des Sciences*, 1962. **255**(16): p. 1893-&.
22. Benninghoven, A., *Z. Phys. ;230: 403-17(1970).* 1970.
23. Wittmaack, K., *Review of Scientific Instruments*, 1976. **47**(1): p. 157-158.
24. Muller, U., M. Schittenhelm, R. Schmittgens, and H. Helm, *Surface and Interface Analysis*, 1999. **27**(10): p. 904-+.
25. Sodhi, R.N.S., *Analyst*, 2004. **129**(6): p. 483-7.

26. Liu, R. and A.T.S. Wee, *Applied Surface Science*, 2004. **231**: p. 653-657.
27. Gilmore, I.S. and M.P. Seah, *Applied Surface Science*, 2002. **187**(1-2): p. 89-100.
28. Gilmore, I.S. and M.P. Seah, *Applied Surface Science*, 2003. **203-204**: p. 600-604.
29. Davies, M.C., R.D. Short, M.A. Khan, J.F. Watts, A. Brown, A.J. Eccles, P. Humphrey, J.C. Vickerman, and M. Vert, *Surface and Interface Analysis*, 1989. **14**(3): p. 115-120.
30. Iltgen, K., C. Bendel, A. Benninghoven, and E. Niehuis, *Journal of Vacuum Science & Technology a-Vacuum Surfaces and Films*, 1997. **15**(3): p. 460-464.
31. Cheng, J., A. Wucher, and N. Winograd, *Journal of Physical Chemistry B*, 2006. **110**(16): p. 8329-8336.
32. Weibel, D., S. Wong, N. Lockyer, P. Blenkinsopp, R. Hill, and J.C. Vickerman, *Analytical Chemistry*, 2003. **75**(7): p. 1754-1764.
33. Piwowar, A.M. and J.C. Vickerman, *Surface and Interface Analysis*, 2010. **42**(8): p. 1387-1392.
34. Touboul, D., F. Kollmer, E. Niehuis, A. Brunelle, and O. Laprevote, *Journal of the American Society for Mass Spectrometry*, 2005. **16**(10): p. 1608-1618.
35. Davies, N., D.E. Weibel, P. Blenkinsopp, N. Lockyer, R. Hill, and J.C. Vickerman, *Applied Surface Science*, 2003. **203**: p. 223-227.
36. Gillen, G. and S. Roberson, *Rapid Communications in Mass Spectrometry*, 1998. **12**(19): p. 1303-1312.
37. Gillen, G., R.L. King, and F. Chmara, *Journal of Vacuum Science & Technology A: Vacuum, Surfaces, and Films*, 1999. **17**(3): p. 845-852.
38. Boschmans, B., P. Van Royen, and L. Van Vaeck, *Rapid Communications in Mass Spectrometry*, 2005. **19**(18): p. 2517-2527.
39. Szakal, C., S.M. Hues, J. Bennett, and G. Gillen, *The Journal of Physical Chemistry C*, 2009. **114**(12): p. 5338-5343.
40. Shard, A.G., P.J. Brewer, F.M. Green, and I.S. Gilmore, *Surface and Interface Analysis*, 2007. **39**(4): p. 294-298.
41. Kersting, R., B. Hagenhoff, F. Kollmer, R. Mollers, and E. Niehuis, *Applied Surface Science*, 2004. **231**: p. 261-264.
42. Lee, J.L.S., I.S. Gilmore, and M.P. Seah, *Private unpublished communication*, 2011.
43. Fahey, A.J. and S. Messenger, *International Journal of Mass Spectrometry*, 2001. **208**(1-3): p. 227-242.
44. Stephan, T. *Statistical analysis of single-ion-counting data and isotopic measurements with TOF-SIMS*. in *SIMS VIII*. 1992. Munster: John Wiley & Sons.
45. Stephan, T., J. Zehnpfenning, and A. Benninghoven, *Journal of Vacuum Science & Technology a-Vacuum Surfaces and Films*, 1994. **12**(2): p. 405-410.
46. Norrman, K., A. Papra, F.S. Kamounah, N. Gadegaard, and N.B. Larsen, *Journal of Mass Spectrometry*, 2002. **37**(7): p. 699-708.
47. Ratner, B.D., *Biomaterials science: an introduction to materials in medicine*. 1996: Academic Press.
48. Briggs, D., *XPS:Basic Principles, Spectral Features and Quantitative Analysis*, in *Surface Analysis by Auger and X-ray Photoelectron Spectroscopy*, D. Briggs and J.T. Grant, Editors. 2003, IM Publications and Surface Spectra Ltd: Chichester and Manchester. p. 31-56.

49. Briggs, D., *Surface analysis of polymers by XPS and static SIMS*. 1998, Cambridge: Cambrige University Press. 198.
50. Tyler, B.J., D.G. Castner, and B.D. Ratner, *Journal of Vacuum Science & Technology a-Vacuum Surfaces and Films*, 1989. **7**(3): p. 1646-1654.
51. Briggs, D. and M.P. Seah, *Practical Surface Analysis*. Vol. 1. 1990, Chichester: John Wiley & Sons, Ltd.
52. Wiza, J.L., *Nuclear Instruments & Methods*, 1979. **162**(1-3): p. 587-601.
53. Beamson, G. and D. Briggs, *High Resolution XPS of Organic Polymers - The Scienta ESCA300 Database*. 1992, Chichester: Wiley.
54. Miyayama, T., N. Sanada, S.-i. Iida, J.S. Hammond, and M. Suzuki, *Applied Surface Science*, 2008. **255**(4): p. 951-953.
55. Tanaka, K., N. Sanada, M. Hikita, T. Nakamura, T. Kajiyama, and A. Takahara, *Applied Surface Science*, 2008. **254**(17): p. 5435-5438.
56. Rafati, A., M.C. Davies, A.G. Shard, S. Hutton, G. Mishra, and M.R. Alexander, *Journal of Controlled Release*, 2009. **138**(1): p. 40-44.
57. Bachman, B.J. and M.J. Vasile, *Journal of Vacuum Science & Technology A: Vacuum, Surfaces, and Films*, 1989. **7**(4): p. 2709-2716.
58. Vickerman, J.C., *Surface Analysis: The Principal Techniques*. 2003: John Wiley & Sons Ltd.
59. Tyler, B.J., G. Rayal, and D.G. Castner, *Biomaterials*, 2007. **28**(15): p. 2412-2423.
60. Lee, J.L.S., I.S. Gilmore, I.W. Fletcher, and M.P. Seah, *Surface and Interface Analysis*, 2009. **41**(8): p. 653-665.
61. Wagner, M.S., D.J. Graham, B.D. Ratner, and D.G. Castner, *Surface Science*, 2004. **570**(1-2): p. 78-97.
62. Lee, J.L.S., I.S. Gilmore, and M.P. Seah, *Surface and Interface Analysis*, 2008. **40**: p. 1-14.
63. Lee, J.L.S. and I.S. Gilmore, *The application of multivariate data analysis techniques in surface analysis*, in *Surface Analysis The Principal Techniques*, J.C. Vickerman and I.S. Gilmore, Editors. 2009, John Wiley & Sons: London.
64. Fujiwara, H., *Spectrescopic Ellipsometry: Principles and applications*, ed. H. Fujiwara. 2007, London: Wiley-Blackwell.
65. Langmuir, I. and V.J. Schaefer, *Journal of the American Chemical Society*, 1937. **59**: p. 1406-1406.
66. Walker, M.L., D.J. Vanderah, and K.A. Rubinson, *Colloids Surf B Biointerfaces*, 2011. **82**(2): p. 450-5.
67. Herrwerth, S., W. Eck, S. Reinhardt, and M. Grunze, *Journal of the American Chemical Society*, 2003. **125**(31): p. 9359-9366.
68. Kodera, S., T. Okajima, H. Iwabuki, D. Kitaguchi, S. Kuroda, T. Yoshinobu, K. Tanizawa, M. Futai, and H. Iwasaki, *Analytical Biochemistry*, 2003. **321**(1): p. 65-70.
69. Santos, O., T. Nylander, M. Paulsson, and C. Tragardh, *Journal of Food Engineering*, 2006. **74**(4): p. 468-483.
70. Raman, C.V. and K.S. Krishnan, *Nature*, 1928. **121**: p. 501-502.
71. Gardiner, D.J., *Practical Raman Spectroscopy*, ed. P.R. Graves. 1989: Springer.
72. Pemble, M.E. and P. Gardner, *Vibrational Spectroscopy from Surfaces*, in *Surface Analysis The Principal Techniques*, J.C. Vickerman and I.S. Gilmore, Editors. 2009, John Wiley & Sons: London.

73. Davies, M.C., J.S. Binns, C.D. Melia, P.J. Hendra, D. Bourgeois, S.P. Church, and P.J. Stephenson, *International Journal of Pharmaceutics*, 1990. **66**(1-3): p. 223-232.
74. Day, J.S., H.G.M. Edwards, S.A. Dobrowski, and A.M. Voice, *Spectrochimica Acta Part a-Molecular and Biomolecular Spectroscopy*, 2004. **60**(8-9): p. 1725-1730.
75. Tabaksblat, R., R.J. Meier, and B.J. Kip, *Applied Spectroscopy*, 1992. **46**(1): p. 60-68.
76. Hecht, L., L.D. Barron, and W. Hug, *Chemical Physics Letters*, 1989. **158**(5): p. 341-344.
77. Barron, L.D., L. Hecht, W. Hug, and M.J. MacIntosh, *Journal of the American Chemical Society*, 1989. **111**(23): p. 8731-8732.
78. WiTec, *Confocal Raman Microscope CRM 200*. 2011.
79. Smith, G.E., *Nuclear Instruments and Methods in Physics Research Section A: Accelerators, Spectrometers, Detectors and Associated Equipment*, 2009. **607**(1): p. 1-6.
80. Tompsett, M.F., G.F. Amelio, W.J. Bertram, R.R. Buckley, W.J. McNamara, Mikkelse.Jc, and D.A. Sealer, *Ieee Transactions on Electron Devices*, 1971. **ED18**(11): p. 992-&.
81. Robbins, M.S. and B.J. Hadwen, *Ieee Transactions on Electron Devices*, 2003. **50**: p. 1227-1232.
82. Binnig, G., C.F. Quate, and C. Gerber, *Physical Review Letters*, 1986. **56**(9): p. 930-933.
83. Fechner, P., T. Boudier, S. Mangenot, S. Jaroslawski, J.N. Sturgis, and S. Scheuring, *Biophysical Journal*, 2009. **96**(9): p. 3822-3831.
84. Vansteenkiste, S.O., M.C. Davies, C.J. Roberts, S.J.B. Tendler, and P.M. Williams, *Progress in Surface Science*, 1998. **57**(2): p. 95-136.
85. Ellis, J.S., S. Allen, Y.T.A. Chim, C.J. Roberts, S.J.B. Tendler, and M.C. Davies, *Polymer Therapeutics Ii: Polymers as Drugs, Conjugates and Gene Delivery Systems*, 2006. **193**: p. 123-172.
86. Vansteenkiste, S.O., M.C. Davies, C.J. Roberts, and S.J.B. Tendler, *Progress in Surface Science*, 1998. **57**(2): p. 95-136.
87. Jalili, N. and K. Laxminarayana, *Mechatronics*, 2004. **14**: p. 907-945.
88. Hamers, R.J., *Journal of Physical Chemistry*, 1996. **100**: p. 13103-13120.
89. Leggett, G.J., *Analytica Chimica Acta*, 2003. **479**: p. 17-38.
90. Hugel, T. and M. Seitz, *Macromolecular Rapid Communications*, 2001. **22**(13): p. 989-1016.
91. Pittenger, B., N. Erina, and C. Su, *Quantitative Mechanical Property Mapping at the Nanoscale with PeakForce QNM*. 2010, Veeco.
92. Davies, M.C., C.J. Roberts, S.J.B. Tendler, and P.M. Williams, *The Surface Analysis of Polymeric Biomaterials*, in *Biocompatibility: Assessment of Materials and Devices for Medical Applications*, J. Braybrook, Editor. 1997, John wiley and Sons Ltd. p. 65-100.
93. Hansma, H.G., K.J. Kim, D.E. Laney, R.A. Garcia, M. Argaman, M.J. Allen, and S.M. Parsons, *Journal of Structural Biology*, 1997. **119**(2): p. 99-108.